

Energy distribution and adiabatic guiding of a solid-neon-moderated positron beam

S Ghosh¹ , J R Danielson  and C M Surko 

Department of Physics, University of California San Diego, La Jolla, CA 92093, United States of America

E-mail: soumen@physics.ucsd.edu, jdan@physics.ucsd.edu and csurko@ucsd.edu

Received 24 October 2019, revised 3 February 2020

Accepted for publication 13 February 2020

Published 24 March 2020



CrossMark

Abstract

Slow positrons are generated from a ^{22}Na source and cone-shaped solid neon moderator and extracted as a magnetically guided beam. Measurements are presented for the mean parallel and perpendicular energies and the radial distribution of the beam particles. Over a distance of 7 m, where the magnetic field B varies from 0.005 to 0.12 T, the beam transport is found to be adiabatic for mean energies up to 50 eV. Non-adiabatic effects, evidenced by an increase in energy in motion perpendicular to B , are observed at larger transport energies. The implications of these observations for buffer-gas positron traps and other positron-transport beamlines are discussed.

Keywords: positron beam transport, neon moderator, adiabatic invariance, energy distribution

1. Introduction

The interaction of low-energy positrons with matter are important in many areas, including atomic and molecular physics, material science, astrophysics, and medicine [1–4]. However, much less is known about positron interactions with matter as compared with analogous electron interactions. This is primarily due to the difficulties in obtaining sufficient numbers of positrons for such studies.

Positrons for laboratory experiments can be obtained from radioisotopes or from electron–positron (‘pair’) production due to bremsstrahlung of accelerated electron beams [5, 6]. In both cases, they have a broad energy spectrum (e.g. hundreds of keV) which frequently must be reduced to lower mean energies ($\sim\text{eV}$) before they are useful for atomic physics and other studies. This is typically achieved by allowing them to lose energy in a ‘moderator’ material [7, 8]. A key consideration determining the combined source and moderator utility is the extent of the emitted slow positrons in phase space; namely the spatial extent and distribution in velocity space, which can vary considerably based on the moderator material.

Many materials have been used to produce slow positrons in vacuum, including single-crystal or polycrystalline metals (e.g. tungsten, copper or nickel) [9–12] and thin layers

of a rare-gas solid at cryogenic temperatures [13–17]. The major difference between metal and rare-gas moderators is that metals provide better energy resolution than the solid rare gases [18], but rare gases are more efficient [19–22]. Solid neon has been found to have the highest efficiency of any moderator developed to date. This efficiency depends upon moderator geometry. In particular, a conical shape is preferable to a cup [18], and so the former arrangement is now used extensively.

The combination of a ^{22}Na radioisotope source and solid-neon moderator is very well suited for operation with buffer-gas positron traps (BGT). In this case, positrons with appreciable energy spread (e.g. $\Delta E \sim \pm 2\text{ eV}$) can be captured efficiently, while the beam exiting the trap has a much smaller energy spread ($\Delta E \leq 50\text{ meV}$). Such BGTs are now used worldwide in a variety of experiments, including the creation and study of antihydrogen [23–26] and dense gases of positronium (Ps) atoms [27], formation and study of the positronium molecule [28], scattering and annihilation experiments [29, 30], and the creation of a new generation of Ps beams [31–33].

In spite of their utility, there have been few systematic studies of the beam-energy and spatial distributions of slow positrons from neon cone moderators and of the parameters that determine the quality of the resulting positron beam. A better understanding of the spatial and energy distribution (i.e. the mean parallel and perpendicular energies) of the moderated beam can be expected to increase the utility of such sources for

¹ Author to whom any correspondence should be addressed.

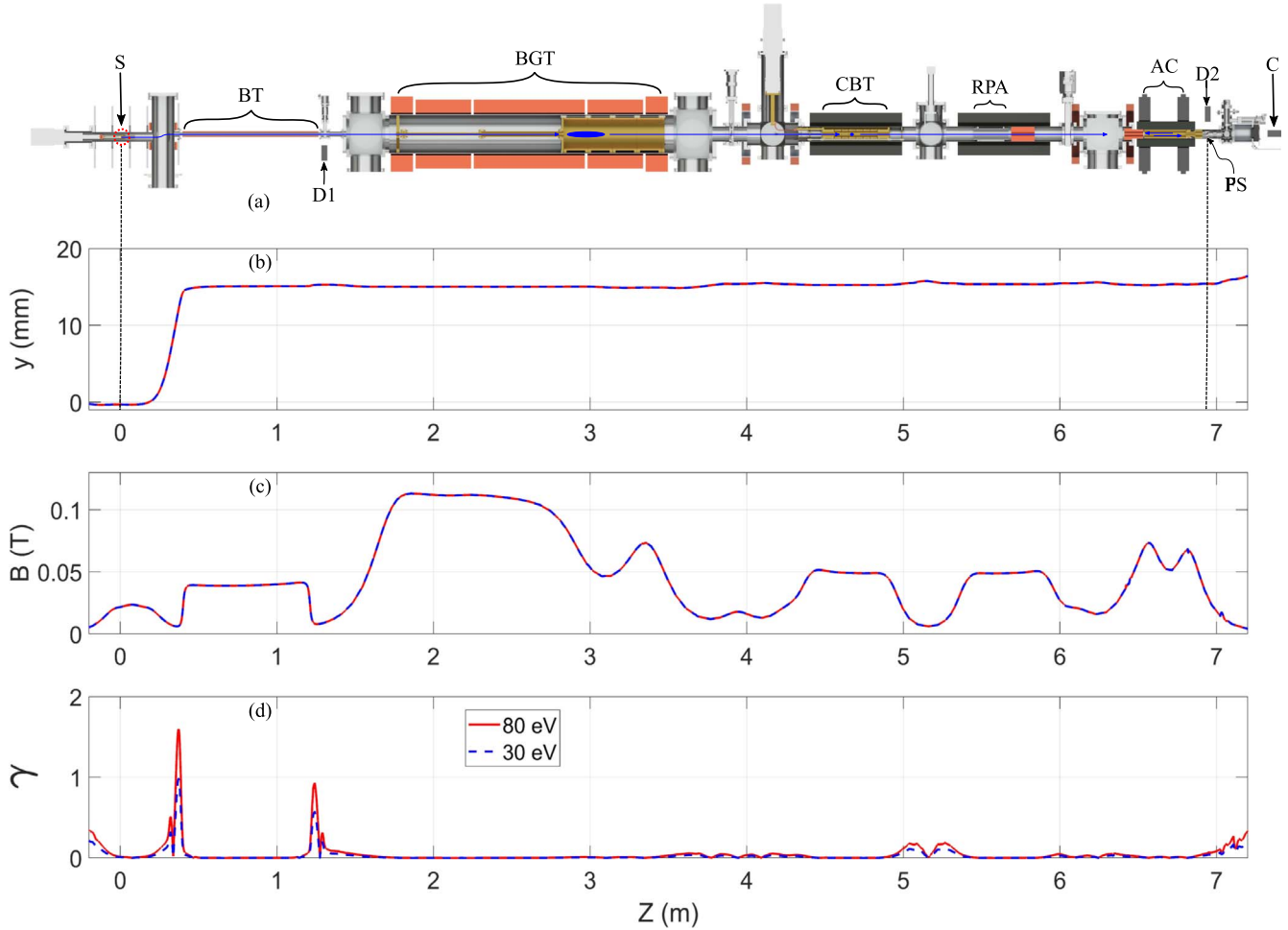


Figure 1. (a) Schematic of the positron beam line showing the ^{22}Na source (S), beam tube (BT), buffer gas trap (BGT), cryogenic beam-tailoring trap (CBT), retarding potential analyzer (RPA), annihilation cell (AC), gamma-ray detectors D_1 and D_2 , CCD camera (C) and phosphor screen (PS). (b) Height of the beamline from the center of the source to the phosphor screen; (c) the total magnetic field B along this flux line; and (d) the calculated adiabatic parameter γ . The red solid lines and blue dash lines in (d) correspond to 80 and 30 eV positrons respectively.

a number of applications, particularly those employing BGTs [34]. In particular, the most useful beams will have small transverse spatial extent and a narrow energy spread in both the perpendicular and parallel directions to the magnetic field, either when used alone or to feed BGTs.

Many techniques have been developed over the years to study the energy distributions of magnetically guided electron beams from various sources (e.g. [35–37]). Typically these beams have much higher currents (μA to mA , compared to the sub- pA currents from the typical positron beam source), and so many electron-beam analysis techniques are not possible for positron beams. However, virtually all of them rely on the use of the magnetic-moment adiabatic invariant to investigate the underlying energy distribution.

Presented here is a study of slow positron beam formation and measurements of both the mean parallel and perpendicular energies of a magnetically guided beam from a ^{22}Na source and solid-Ne cone moderator. The radial distribution of the beam is measured and placed on an absolute scale relative to the point of emission at the moderator cone. The important role of adiabaticity in analyzing the beam energy distribution is also studied.

This paper is organized as follows. Section 2 discusses the experimental details, including description of the source and cone moderator. Section 3 discusses the regime of adiabatic positron transport in the beam line and measurements that it enables. Section 4 describes measurements and analysis for the spatial and energy distributions of the beam, and section 5 discusses nonadiabatic transport effects and the role they play in modifying the beam energy distribution. The paper ends with a summary and some concluding remarks.

2. Experimental details

2.1. Source and cone moderator

As shown in in figure 1, the sealed ^{22}Na radioactive source (activity $\sim 6 \text{ mCi}^2$) is placed next to a gold-plated Cu cone-shaped cap (figure 2). The cone and source are attached to the second stage ($\sim 8 \text{ K}$) of a cryo-cooler by a sapphire washer

² The Source was Purchased from iTemba Labs (National Science Foundation, South Africa), It was Originally 50 mCi in Strength and Encased in their ‘Small-Capsule’ Container.

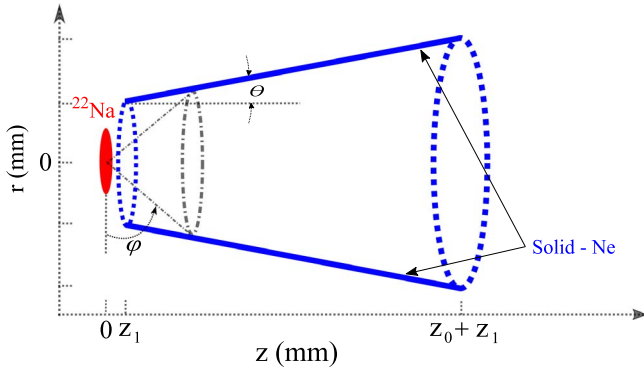


Figure 2. Schematic diagram of the ^{22}Na source (red filled circular section with thickness 0.1 mm and sealed using an $8\ \mu\text{m}$ thick titanium window) and cone-shaped moderator with the location and frozen Ne gas on the surface indicated in blue. The cone angle $\theta = 10.3^\circ$. The height of the conical section is $z_0 = 11\ \text{mm}$, and the radius r varies from 2 to 4 mm. The source is located $z_1 = 1.3\ \text{mm}$ from the base of the cone [39].

which provides good thermal conductivity and electrical insulation. This permits electrical biasing of the moderator, which in turn sets the energy of the slow positrons extracted from the moderator. The cone and source are placed inside a Cu heat shield which is attached to the first stage of the cryocooler ($\sim 50\ \text{K}$). Neon gas is injected through a small hole in the heat shield and freezes on the cone. The Ne gas pressure is controlled via a piezoelectric valve. The Ne gas is allowed to flow for few minutes (product of pressure times time $\sim 10\ \text{mTorr min}$). This empirically determined procedure is found to give the highest flux of slow positrons. Approximately 2 mTorr for 5 min yields $\sim 1 \times 10^6\ e^+/\text{s}$ (efficiency $\sim 0.5\%$ which is typical for these sources [20, 38]).

2.2. The positron beam line

Slow positrons from the moderator are magnetically guided. They have energy spreads of a few electron volts FWHM [20, 40]. Using this beam as input, BGT based positron beams have been developed with significant improvements in beam energy resolution [41, 42] as compared, for example, to remoderated beams using Ni(100) crystal at 77 K [43]. The apparatus used here is shown in figure 1. The source and moderator are connected to a beam tube and gate valve. A gamma-ray detector measures the flux of moderated positrons when they annihilate on the closed gate valve (D1 in figure 1(a)).

Besides the moderated positrons, high-energy positrons that are not moderated (e.g. $>1\ \text{keV}$) are also emitted by the source. A small vertical magnetic field is used to raise the center of the beamline after the moderator (figure 1(b)) to filter them out. The energetic positrons fail to follow the field and annihilate on the chamber walls.

The beam is then magnetically guided through a BGT, a cryogenic BGT, a retarding potential analyzer (RPA), an annihilation cell, and finally to a phosphor screen. Other than using the RPA for the energy measurements described below, none of the other elements after the beam monitor D1 and before the phosphor screen are used for the experiments described here.

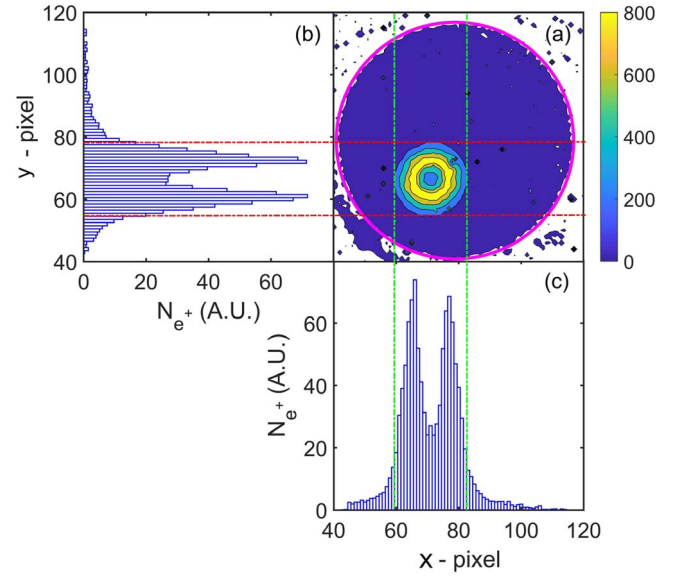


Figure 3. (a) Image of the luminescence on the phosphor screen for beam transport energy of 30 eV. The magenta circle is the periphery of the screen (diameter 19 mm; pixel size 0.32 mm). The intensity distribution indicates that an annular positron beam distribution is generated from the cone moderator. (b) and (c) are the vertical and horizontal slice passing through the center of the annulus. The peak to peak distance gives an annulus diameter of $4.0 \pm 0.3\ \text{mm}$. The red and green dash-dot lines indicate the outer edges of the moderator cone ($\pm 4\ \text{mm}$ in figure 2). The low-intensity pattern outside this region is likely due to diffuse light from the luminescence [47].

2.3. Phosphor screen and camera

The slow positrons follow the magnetic field, since the positron gyro-radius (e.g. $\rho_{e^+} \sim 0.1\ \text{mm}$ for 1 eV perpendicular energy at 30 mT) is much smaller than the spatial scale of the cone (i.e. $\sim \text{mm}$). A phosphor screen is located $\sim 6.9\ \text{m}$ from the source. The CCD camera is focused on the screen through a view port at the end of the beam line. The screen is electrically biased at +6 V to prevent loss of secondary electrons. The camera detects the luminescence produced when positrons impinge on the screen [44]. As discussed in detail below, an annular pattern is observed as indicated in figure 3. This is qualitatively similar to ring-shaped patterns observed previously from neon cone moderators [17, 38, 45, 46].

2.4. Retarding potential analyzer

The RPA, shown in figure 1(a), is a cylindrical electrode with aspect ratio (length to diameter) ~ 3 . It is used to obtain details of the parallel energy distribution of the beam; and in particular, to measure the mean and standard deviation, \bar{E}_{\parallel} and σ_{\parallel} , of the parallel energy.

A sequence of integrated camera images of the transmitted beam is obtained. For each image, the RPA is first set to a static voltage while the beam is blocked upstream. The camera is then triggered, the blocking voltage is removed, and the light integrated for 60 s, after which the blocking voltage is reapplied. The RPA voltage is then changed, and the process is repeated. Poloidal averages (i.e. circular rings on the

phosphor screen) are then performed. Adding all rings together gives the total luminance. The charge on the phosphor screen is also measured using a charge-sensitive amplifier to get the absolute positron flux, and this is used to calibrate the luminescence signal. A second gamma-ray detector (D2 in figure 1(a)) is located perpendicular to the phosphor screen. It detects the gamma rays from positron annihilation on the screen and is also used to measure the total positron number.

3. Adiabatic positron transport

In a spatially varying magnetic field, when the time variation of the field is slow in the frame of the moving particle, the magnetic moment

$$\mu = \frac{\bar{E}_\perp}{B} \quad (1)$$

is an adiabatic invariant, where \bar{E}_\perp is the energy associated with the positron gyro-motion [48]. An adiabaticity parameter γ can be defined as the fractional change in B in one positron gyration in the field [49] e.g.

$$\gamma = \frac{\tau_c}{B} \frac{dB}{dt} = \frac{2\pi m v_z}{eB} \frac{dB}{dz}, \quad (2)$$

with $\tau_c = 2\pi/\omega_c$, where $\omega_c = eB/m$ is the cyclotron frequency, $v_z = \sqrt{2\bar{E}_\parallel/m}$, and m and e are the positron mass and charge. Thus

$$\gamma = \frac{2\pi\sqrt{2m\bar{E}_\parallel}}{eB^2} \frac{dB}{dz}, \quad (3)$$

where \bar{E}_\parallel is the component of positron energy associated with motion parallel to the magnetic field. Qualitatively, adiabatic positron transport will hold if $\gamma \ll 1$ and be broken when $\gamma \gg 1$.

Measurement of \bar{E}_\perp variations as a function of beam energy, while keeping the source magnetic field (B_s) constant, can be used to study adiabatic invariance. Such an analysis for a room temperature (25 meV) BGT-based positron beam is discussed in [50, 51]. In that work, measurement of the perpendicular energy was used to measure the cooling of positrons in a buffer-gas-trap and to investigate ways to minimize the energy spread of the ejected beam. In that context, the \bar{E}_\parallel and \bar{E}_\perp distributions were well described by Gaussian and Maxwell–Boltzmann distributions respectively.

The total beam energy distribution $f(E_t)$ was obtained by convolving the joint energy distribution of parallel and perpendicular energies $f(E_\parallel, E_\perp)$ with an energy conserving delta function $\delta(E_\parallel + E_\perp - E_t)$. The result was an exponentially-modified Gaussian distribution (EMG) (equation (5) of [50]), although the parallel and perpendicular energy distributions can change along the beam path, the total energy distribution will be a constant, since the changing magnetic field cannot alter the energies of the particles, only redistribute it between the motion parallel and perpendicular to B .

The moderated positron beam experiences variations in B over the 7 m path. Adiabatic transport and equation (1) imply

$$\frac{\bar{E}_{\perp R}}{B_R} = \frac{\bar{E}_{\perp S}}{B_S} \Rightarrow \bar{E}_{\perp R} = M\bar{E}_{\perp S}, \quad (4)$$

where $M \equiv B_R/B_S$ is the magnetic mirror ratio, $\bar{E}_{\perp S}$ and $\bar{E}_{\perp R}$ are the mean perpendicular energies at the moderator (source) and RPA. Conservation of energy implies

$$\bar{E}_t = \bar{E}_{\parallel R} + \bar{E}_{\perp R}, \quad (5)$$

where $\bar{E}_{\parallel R}$ is the mean parallel energy at the RPA. Substituting equation (4) into energy conservation equation (5), results in the following linear dependence of $\bar{E}_{\parallel R}$ on M

$$\bar{E}_{\parallel R} = (-\bar{E}_{\perp S}) \times M + \bar{E}_t. \quad (6)$$

Thus, in the regime in which adiabatic transport is valid, measurement of $\bar{E}_{\parallel R}$ as a function of M yields a measurement of $\bar{E}_{\perp S}$ (i.e. the slope of the curve).

4. Measurements and analysis

4.1. Radial distribution

An example of the luminescent intensity on the phosphor screen for a 30 eV positron beam is shown in figure 3 for a 10 min exposure. The relatively long exposure time enhances a low-intensity background glow and thus enables imaging of the entire phosphor screen. When combined with the known magnetic field ratio between the source and the phosphor screen, this permits a spatial calibration of the image. The total luminescence is calibrated with an absolute charge measurement to obtain the total positron number. The image in figure 3 indicates that the radial distribution is a hollow annulus, with a peak radius ~ 2.0 mm, which corresponds closely to the minimum radius of the moderator cone (see figure 2).

It is believed that all positrons originate from the region inside the maximum radius of the conical section, $r = 4$ mm. Thus, the origin of the low-intensity glow outside the moderator cone is unknown. It could be scattered light *inside* the phosphor screen at regions of intense light emission. This is related to the process of ‘veiling glare’ which is common in high-contrast images using phosphor screens [47].

Radial distributions of the areal (i.e. 2D) positron density n_{e^+} are shown figure 4, as the RPA voltage is varied, for 30 and 80 eV beam transport energies for 60 s exposure times. They are obtained by locating the image center and azimuthally averaging the values at each radius. These distributions are found to be approximately self-similar as the RPA voltage is varied for beam energies from 10 to 80 eV. This is illustrated in figures 4(e) for 30 eV and (f) for 80 eV, where the area normalized data collapse to a single line. Here, data for positron number $< 15\%$ were not included because of poorer signal to noise. The radial distributions peak at or very near the inner radius of the cone. The self-similar nature of the radial distributions, independent of RPA bias, indicates that the mean parallel and perpendicular energies are

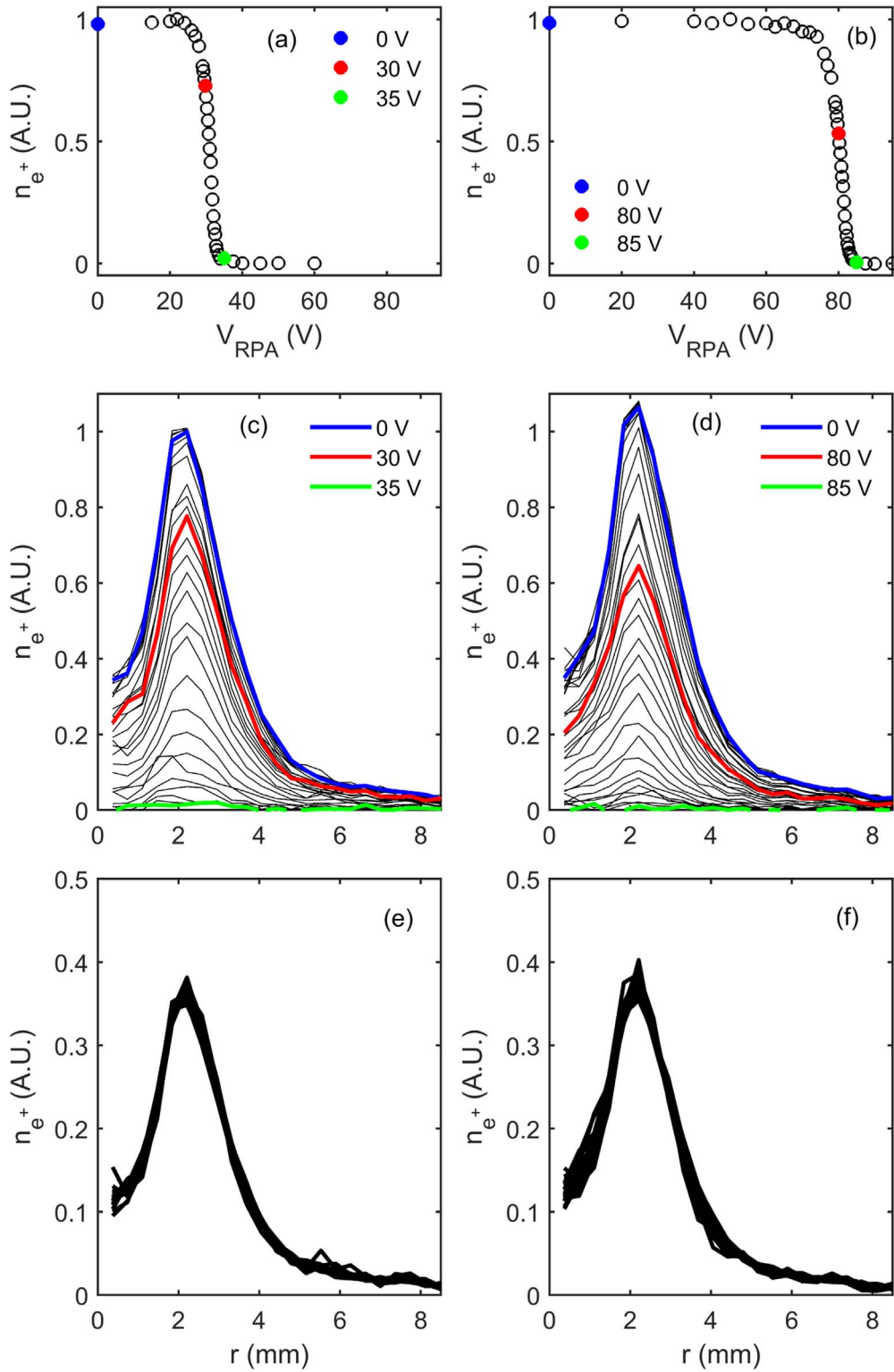


Figure 4. RPA data are shown for (a) 30 eV and (b) 80 eV beam transport energies for $M = 2.3$. The respective radial distributions of areal positron density n_{e^+} are shown in (c) and (d) for V_{RPA} varying from 0 to 60 V and 0 to 95 V (top to bottom). Blue, red and green curves are the radial distributions for 0, 30, 35 V in (a) and 0, 80, 85 V in (b). Area-normalized radial profiles are shown in (e) and (f) for V_{RPA} values that transmit $\geq 15\%$ positrons for the 30 and 80 eV beams.

approximately the same at any radial location. This appears to be true whether positrons emanate from flat surface of the source or the cone.

As observed above, a distinctive feature of the spatial distribution is that it peaks at the inner radius of the cone, $r = 2$ mm. We note that a simple model (albeit with sweeping

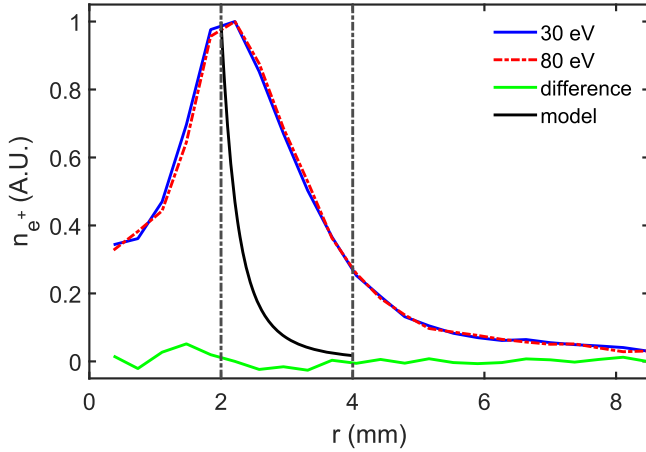


Figure 5. Blue solid and red dash–dot lines are the areal positron density profiles (peak normalized) at $V_{\text{RPA}} = 0$ V for the 30 and 80 eV beams respectively with the difference indicated by the green line. The vertical black dash–dot lines indicate the minimum and maximum cone radii of 2 and 4 mm. The black solid curve is the prediction of equation (9).

assumptions) predicts such a peak. Assuming an isotropic point source of positrons at axial location z_1 in figure 2, the flux N_{e^+} of positrons impinging on an annular region of the cone at angle ϕ in the region between radii r and $r + dr$ (coordinates defined in figure 2) will be

$$dN_{e^+} = C \frac{d\phi}{dr} dr, \quad (7)$$

with

$$\phi = \tan^{-1} \left[\frac{z_1 + \left(\frac{z_0}{b-a}\right)(r-a)}{r} \right], \quad (8)$$

where C is a constant, $a = 2$ mm and $b = 4$ mm are the small and large radii and $z_0 = 11$ mm is the height of the conical-section moderator, and the source is located $z_1 = 1.3$ mm from its base, as shown in figure 2.

The areal density of positrons n_{e^+} , to be compared with the measurements in figure 5, will be

$$n_{e^+} = \frac{1}{2\pi r} \frac{dN_{e^+}}{dr} = \frac{1}{2\pi r} C \frac{d\phi}{dr}. \quad (9)$$

This distribution is plotted as the solid black line in figure 5. It shows a very sharp peak at the inner radius of the cone. This reflects the fact that the solid angle of source emission subtended by an annular region on the cone surface peaks sharply at the narrowest portion of the cone. If this consideration dominates the pattern of re-emitted (moderated) positrons, that would help to explain the annular pattern of positron emission from the moderator. However, it still remains an open question as to the origin of the flux for $r \leq 2$ mm and the broadening of the distribution at larger radii.

Radial profile data for the 30 eV and 80 eV beams are compared in detail in figure 5. The difference between these curves is shown as the green line. The maximum difference is $<5\%$, and the root mean square (rms) difference is 1.2%. The total integrated light intensity as a function of exposure time is found to have rms fluctuations $\sim 2\%$ for exposures from 30

to 300 s. For any given individual slice, a jitter of about 1 pixel in the center, would lead to another maximum error of $\sim 5\%$. However, the poloidal averaging used here limits the total average error to $\sim 2\%$. Thus, the measured small deviations appear to be at the level of our measurement uncertainty. This indicates that the positron emission from the moderator is independent of the moderator bias at these energies to within the inherent fluctuations of our experiment. Integrating the curves in figure 5, the total number of positrons coming from $r = 0$ –8.5 mm and comparing it with that from various regions shows that 89% come from $r = 0$ –4 mm and 63% from $r = 2$ –4 mm (i.e. the region of the copper cone). These measurements are expected to provide important ingredients for models of slow positron emission from rare-gas moderators.

4.2. Energy distributions

The beam energy distribution is measured at the RPA, which is more than 5 m from the source, after the beam has traversed a wide range of magnetic fields. As long as the transport in the region where the RPA B field is varied is adiabatic, the measured distribution will accurately reflect the beam distribution at the RPA location. It was noted previously [49], that this particular beamline exhibits adiabatic transport from the BGT to the phosphor screen for transport energies <100 eV, so all measurements in this region are expected to be accurate measurements of the local energy distribution. However, for the measurements to be a faithful reproduction of that at the source, the beam must maintain adiabaticity along the entire path. As discussed in the next section, the region between the source and the BGT has, until now, not been investigated, and will be shown to violate the adiabaticity assumption for some conditions. The following analysis assumes adiabatic positron transport is valid, which is found to be correct in an important range of beam transport energies. The breaking of this invariant will be discussed in the next section.

The total number of detected positrons at the phosphor screen for 60 s integration times and different RPA bias voltages is plotted in figure 6 for three different magnetic fields at the RPA for beam energies of 20, 30, 70 and 80 eV. For each magnetic field, the RPA data are fitted with EMG distributions (discussed above). We note, however, that while the EMG fits the data reasonably well, it is used here for convenience without any underlying physical motivation.

The derivatives of the RPA cutoff curves give the parallel energy distributions (also plotted in figure 6) and thus provide a measure of the standard deviation $\sigma_{\parallel R}$ and $\bar{E}_{\parallel R}$, and these quantities are plotted in figures 7(a) and (b). At low transport energies, and for $M \sim 1$, the parallel energy spread $\sigma_{\parallel} \sim 1$ eV. If the underlying energy distribution were uncorrelated at the source, then the minimum energy spread would be found at $M = 1$ [50]. However, we do not have enough information to describe the complete distribution. Only the mean and standard deviation are obtained, and so the degree of correlation is unknown. Data at many different magnetic fields (both $M > 1$ and $M < 1$) would be necessary

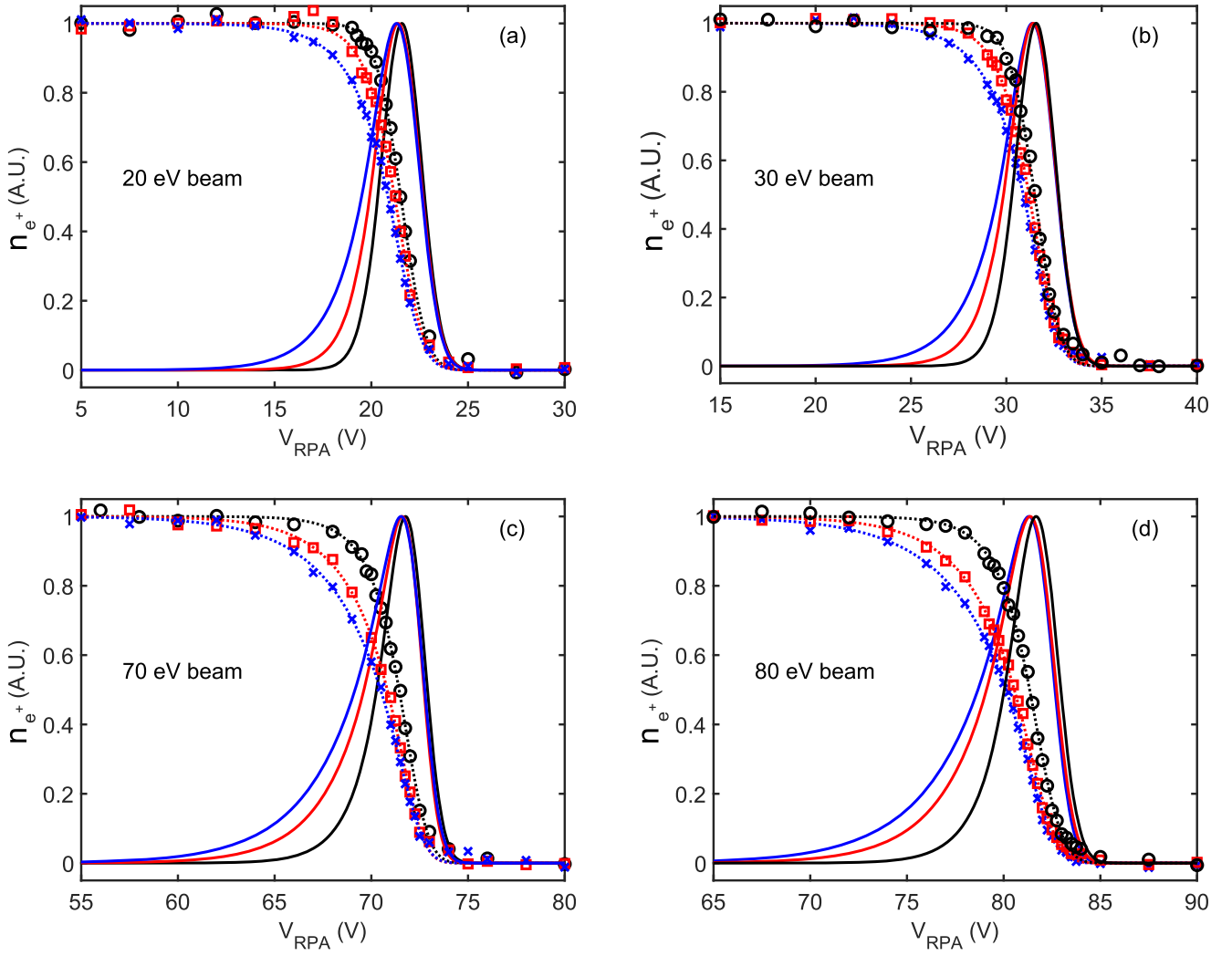


Figure 6. Measured positron number as a function of RPA bias for $M = \frac{B_R}{B_S} = 1.2$ (black circles), $M = 1.7$ (red squares), $M = 2.3$ (blue crosses), for (a) 20 V, (b) 30 V, (c) 70 V, and (d) 80 V bias applied to the moderator. Dotted lines are the EMG fits with respective colors. Data are fit to a 95% confidence level. The derivatives of these fits are the parallel energy distributions at the RPA, represented by the color-coded solid lines. Mirroring is visible as the distributions are skewed towards lower energies as M is increased.

to accurately characterize the true particle distribution at the moderator [50].

To measure the mean perpendicular energies, the mean parallel energies $\bar{E}_{\parallel R}$, obtained from figure 6, are plotted as a function of M , as shown in figure 7(b), varying B_R while keeping B_S constant. As per equations (1) and (4) the slopes of these fits to the data yield the mean perpendicular energies $\bar{E}_{\perp R}$ at the RPA. These results are shown in figure 8, where $\bar{E}_{\perp R}$ is plotted vs the mean parallel energy, with both evaluated at $M = 1$. For situations in which adiabatic invariance holds between the source and the RPA, equation (6) is valid. For $M = 1$, $\bar{E}_{\perp R} = \bar{E}_{\perp S}$ and thus the data provide a measure of the mean perpendicular and parallel energy at the moderator. The difference between the lower and higher transport energies (i.e. 20 and 30 as compared with 70 and 80 eV in figure 8) is interpreted as evidence of a departure from adiabatic invariance upstream of the BGT at the higher energies.

5. Departure from adiabatic invariance

The precise dependence of $\bar{E}_{\perp R}$ on γ depends upon the specific situation. When $\gamma \ll 1$ adiabatic transport is expected, while for $\gamma \gg 1$ adiabaticity is expected to be broken (e.g. see [52, 53]). Generally speaking, it is expected that non-adiabatic changes to the energy will begin to become significant for $\gamma \sim 1$. Examination of equation (3) indicates that such nonadiabatic behavior will occur when B is small and/or \bar{E}_{\parallel} is large.

As shown in figure 1(d), the largest values of γ by far occur at both ends of the narrow beam tube, with the maximum, γ_m , occurring at the location immediately after the moderator. These values are indicated in figure 8. For example, at 30 eV, $\gamma_m = 0.98$ and at 80 eV, $\gamma_m = 1.6$. Referring to the data shown in figure 8, it is seen that $\bar{E}_{\perp R}$ increases from ≈ 0.8 eV at $E = 30$ eV, to ≈ 1.6 eV at

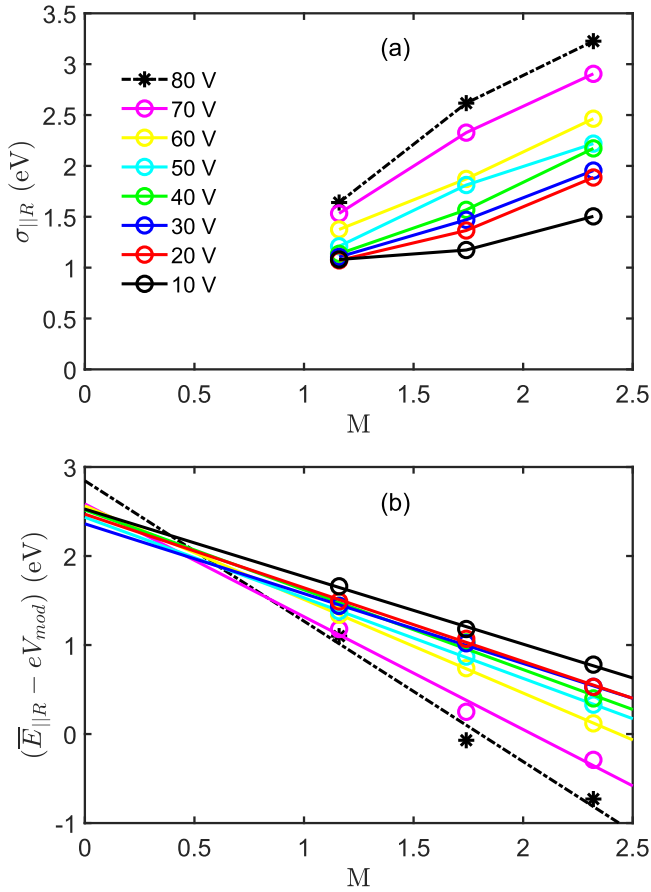


Figure 7. (a) Parallel spreads $\sigma_{\parallel R}$ and (b) mean parallel energy relative to the moderator bias, $\bar{E}_{\parallel R} - eV_{mod}$, from the fitted curves in figure 6 are plotted as a function of the mirror ratio M . Straight-line fits (solid lines) in (b) provide measures of the mean perpendicular energies $\bar{E}_{\perp R}$, and an estimate of the total mean energy from the intercept as $M \rightarrow 0$.

$E = 80$ eV, a factor of two increase, as γ_m increases by a factor of ~ 1.6 .

For mean energies ≤ 50 eV, the mean perpendicular energy is approximately constant at 0.8 ± 0.1 eV, which shows that the energy maintains approximate adiabaticity for $\gamma_m \lesssim 1.3$. For energies above this, the measured beam parameters are not expected to reflect those in the region of the moderator. The fact that the parallel energy spreads $\sigma_{\parallel R}$ shown in figure 7(a) are significantly larger at 70 and 80 eV, as compared with lower energies, is a further consequence of this nonadiabatic redistribution of perpendicular and parallel energy.

6. Summary and concluding remarks

Experimental measurements and analysis have been presented for the parallel and perpendicular energy distributions and the spatial distribution of positrons from a ^{22}Na source and cone-shaped solid-neon moderator. The parallel energy spread σ_{\parallel} of the moderated positron beam is ~ 1 eV. The mean perpendicular energy is comparable, $\bar{E}_{\perp} \sim 0.8$ eV. To our knowledge, this is the first measurement of \bar{E}_{\perp} . For the

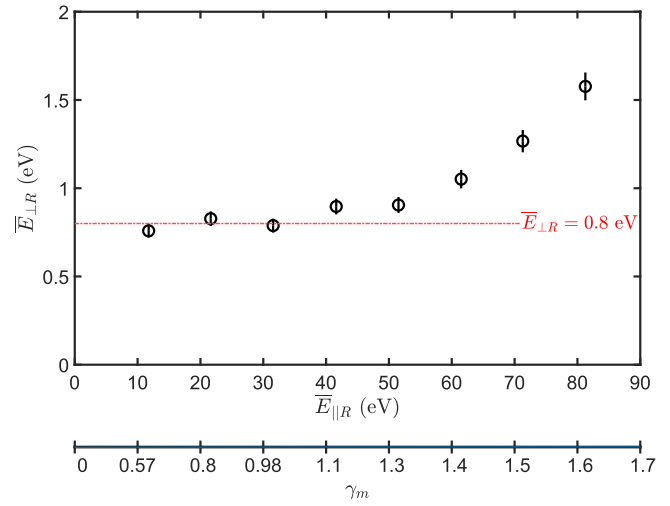


Figure 8. Mean perpendicular energies $\bar{E}_{\perp R}$ at the RPA for different mean parallel energies $\bar{E}_{\parallel R}$ at fixed magnetic field throughout the beam line. The value $\bar{E}_{\perp R} \sim 0.8$ eV for lower beam energies (red dash-dot line is the adiabatic value). Corresponding values of γ_m at specific energies are also indicated.

specific magnetically guided beam studied here, adiabatic positron transport was observed for beam energies in the range 10–50 eV. However, for energies > 50 eV, adiabatic invariance was observed to be broken due to weak magnetic fields and strong gradients at specific locations along the beam line.

The radial distributions at all energies studied (10–80 eV) are very similar, indicating that the adiabatic invariant associated with the guiding-center motion is conserved, even though that associated with the mean perpendicular energy is not [48]. The self-similarity of the energy distributions indicates that the mean parallel and perpendicular energies are the same for any radial location of the cone moderator, irrespective of whether positrons are generated from the flat area above the source (i.e. presumably covered with solid neon) or the moderator-cone surface. Finally, the total number of slow positrons emitted was found to be independent of the moderator bias and the beam transport energy.

These observations highlight the fact that positron moderation in a rare-gas moderator is a complicated process, yet to be understood in detail. For the purposes of optimizing beam transport in a given beam line, measurement of the mean perpendicular and parallel energies, as is done here, is likely sufficient. However, understanding the detailed physics of the moderation process will require more information. Retarding potential measurements over a wider range of magnetic fields would enable a deconvolution to determine the underlying energy distributions both parallel and perpendicular to B . This, and studies with moderators with different cone angles, would provide more detailed information about the actual positron emission process.

Generally speaking, the results presented here are relevant to a wide range of magnetically guided charged-particle-transport beamlines. A key application is use as a positron source to feed BGTs, which are able to accumulate positrons efficiently and cool them to the ambient gas temperature. The

efficiency of these traps depends upon the energy distribution of the incoming positrons. When adiabatic invariance is broken, a moderated positron beam, such as that studied here, will have more \bar{E}_\perp , and this can result in magnetic mirroring, broader parallel energy distributions, and decreased trapping efficiency. Other situations where adiabatic transport is important include positron beams from high-flux sources (e.g. NEPOMUC reactor source [54]), and in cases where the beam must be transported over several meters at low magnetic fields. Here, breaking of the adiabatic invariant can limit the utility of these beams in a number of applications [55, 56]. In these situations, it is important to avoid such nonadiabatic effects.

Acknowledgments

We would like to acknowledge useful conversations with R Greaves, J Machacek, and C Baker. A special acknowledgment also goes to the late Kelvin Lynn, whose many useful and spirited conversations convinced us that there was still more to the story of rare-gas-moderators. This work is supported by US National Science Foundation, Grant No. PHY 17-02230.

ORCID iDs

S Ghosh  <https://orcid.org/0000-0003-2005-2943>

J R Danielson  <https://orcid.org/0000-0002-5904-7976C>

C M Surko  <https://orcid.org/0000-0001-9529-6956>

References

- [1] Gribakin G F, Young J A and Surko C M 2010 *Rev. Mod. Phys.* **82** 2557
- [2] Guessoum N, Jean P and Gillard W 2010 *Mon. Not. R. Astron. Soc.* **402** 1171
- [3] Wahl R L and Buchanan J W 2002 *Principles and Practice of Positron Emission Tomography* (Philadelphia, PA: Lippincott Williams and Wilkins)
- [4] Gidley D W, Peng H G and Vallery R S 2006 *Annu. Rev. Mater. Sci.* **36** 49
- [5] Akahane T, Chiba T, Shiotani N, Tanigawa S, Mikado T, Suzuki R, Chiwaki M, Yamazaki T and Tomimasu T 1990 *Appl. Phys. A* **51** 146
- [6] Oshima N, Suzuki R, Ohdaira T, Kinomura A, Narumi T, Uedono A and Fujinami M 2008 *J. Appl. Phys.* **103** 094916
- [7] Mills A P Jr 1988 *Hyperfine Interact.* **44** 107–24
- [8] Mills A P 2016 *Advances In Atomic, Molecular, and Optical Physics* vol 65 (Cambridge: Elsevier) pp 265–90
- [9] Mills A P 1979 *Appl. Phys. Lett.* **35** 427
- [10] Mills A P Jr 1980 *Appl. Phys.* **23** 189–91
- [11] Coleman P G, Goodyear A and Knights A P 1994 *AIP Conf. Proc.* **303** 218
- [12] Alsulami R, Albarqi M, Jaradat S, Usman S and Graham J 2019 *J. Appl. Phys.* **125** 205304
- [13] Gullikson E M and Mills A P Jr 1986 *Phys. Rev. Lett.* **57** 376
- [14] Gullikson E M, Mills A P Jr and McRae E G 1988 *Phys. Rev. B* **37** 588
- [15] Massoumi G R, Hozhabri N, Lennard W N, Schultz P J, Baert S F, Jorch H H and Weiss A H 1991 *Rev. Sci. Instrum.* **62** 1460
- [16] Weber M, Achwan A, Becker D and Lynn K G 1992 *Hyperfine Interact.* **73** 147–57
- [17] Surko C M, Gilbert S J and Greaves R G 1999 *AIP Conf. Proc.* **498** 3
- [18] Khatri R, Charlton M, Sferlazzo P, Lynn K G, Mills A P Jr and Roellig L O 1990 *Appl. Phys. Lett.* **57** 2374
- [19] Mills A P Jr and Gullikson E M 1986 *Appl. Phys. Lett.* **49** 1121
- [20] Greaves R G and Surko C M 1996 *Can. J. Phys.* **74** 445–8
- [21] Wu Y C, Chen Y Q, Wu S L, Chen Z Q, Wang S J and Greaves R G 2007 *Phys. Status Solidi c* **4** 4032–5
- [22] Lynn K G, Gramsch E, Usmar S G and Sferlazzo P 1989 *Appl. Phys. Lett.* **55** 87
- [23] Jorgensen L V et al 2005 *Phys. Rev. Lett.* **95** 025002–5
- [24] Andresen G B et al 2011 *Nat. Phys.* **7** 558
- [25] Ahmadi M et al 2018 *Nature* **561** 211–5
- [26] Ahmadi M et al 2018 *Nat. Lett.* **557** 71
- [27] Cassidy D B, Deng S H M, Greaves R G and Mills A P 2006 *Rev. Sci. Instrum.* **77** 073106073106–8
- [28] Cassidy D B, Hisakado T H, Tom H W K and Mills A P J 2012 *Optical spectroscopy of molecular positronium* *Phys. Rev. Lett.* **108** 133402133402–5
- [29] Surko C M, Gribakin G F and Buckman S J 2005 Low-energy positron interactions with atoms and molecules *J. Phys. B: At. Mol. Opt. Phys.* **38** R57–126
- [30] Gribakin G F, Young J A and Surko C M 2010 Positron-molecule interactions: resonant attachment, annihilation, and bound states *Rev. Mod. Phys.* **82** 2557
- [31] Jones A C L, Moxom J, Rutbeck-Goldman H J, Osorno K A, Cecchini G G, Fuentes-Garcia M, Greaves R G, Adams D J, Tom H W K and Mills A P 2017 *Phys. Rev. Lett.* **119** 053201
- [32] Michishio K, Chiari L, Tanaka F, Oshima N and Nagashima Y 2019 *Rev. Sci. Instrum.* **90** 023305
- [33] Cassidy D B 2018 Experimental progress in positronium laser physics *Eur. Phys. J. D* **72** 53
- [34] Danielson J R, Dubin D H E, Greaves R J and Surko C M 2015 *Rev. Mod. Phys.* **87** 247
- [35] Orlov D A, Hoppe M, Weigel U, Schwalm D, Terekhov A S and Wolf A 2001 *Appl. Phys. Lett.* **78** 2721
- [36] Devlin L J, Jones L B, Noakes T C Q, Welsch C P and Militsyn B L 2018 *Rev. Sci. Instrum.* **89** 083305
- [37] Karkare S, Feng J, Maxson J and Padmore H A 2019 *Rev. Sci. Instrum.* **90** 053902
- [38] Cooper B S, Alonso A M, Deller A, Wall T E and Cassidy D B 2015 *Rev. Sci. Instrum.* **86** 103101
- [39] Krause-Rehberg R 2019 (Private Communication)
- [40] Danielson J R, Weber T R and Surko C M 2007 *Appl. Phys. Lett.* **90** 081503
- [41] Gilbert S J, Kurz C, Greaves R G and Surko C M 1997 *Appl. Phys. Lett.* **70** 1944
- [42] Natisin M R, Danielson J R and Surko C M 2016 *Appl. Phys. Lett.* **108** 024102
- [43] Gullikson E M and Mills A P Jr 1987 *Phys. Rev. B* **36** 8777
- [44] Stenson E V, Hergenhahn U, Stoneking M R and Pedersen T S 2018 *Phys. Rev. Lett.* **120** 147401
- [45] Sullivan J P, Jones A, Caradonna P, Makochekanwa C and Buckman S J 2008 *Rev. Sci. Instrum.* **79** 113105
- [46] Marjanović S, Banković A, Cassidy D, Cooper B, Deller A, Dujko S and Petrović Z L 2016 *J. Phys. B: At. Mol. Opt. Phys.* **49** 215001
- [47] Flynn M J and Badano A 1999 *J. Digit. Imaging* **12** 50–9
- [48] Bellan P M 2006 *Fundamentals of Plasma Physics* 1st edn (Cambridge: Cambridge University Press)
- [49] Young J A and Surko C M 2006 *Nucl. Instrum. Methods Phys. Res. B* **247** 147–54

- [50] Natisin M R, Danielson J R and Surko C M 2015 *Phys. Plasmas* **22** 033501
- [51] Natisin M R, Danielson J R and Surko C M 2016 *Phys. Plasmas* **23** 023505
- [52] Weber T R, Danielson J R and Surko C M 2010 *Phys. Plasmas* **17** 123507
- [53] Hurst N C, Danielson J R and Surko C M 2015 *Phys. Plasmas* **22** 073503
- [54] Hugenschmidt C, Piochacz C, Reinerand M and Schreckenbach K 2012 *New J. Phys.* **14** 055027
- [55] Stanja J, Hergenbahn U, Niemann H, Paschkowski N, Sunn Pedersen T, Saitoh H, Stenson E V, Stoneking M R, Hugenschmidt C and Piochacz C 2016 *Nucl. Instrum. Methods A* **827** 52–62
- [56] Comeau D *et al* (ATRAP Collaboration) 2012 *New J. Phys.* **14** 045006